

## Research article

# Dynamics of N6-methyladenosine modification during Alzheimer's disease development

Shuai Gao <sup>a,1</sup>, Yuqing Wang <sup>b,c,1</sup>, Xiaoyu Li <sup>a,1</sup>, Yuqing Liang <sup>d,1</sup>, Zhihao Jin <sup>b</sup>, Baozhi Yang <sup>b</sup>, Ti-Fei Yuan <sup>e</sup>, Hengli Tian <sup>d</sup>, Bo Peng <sup>a,f</sup>, Yanxia Rao <sup>b,\*</sup>

<sup>a</sup> Department of Neurosurgery, Huashan Hospital, Institute for Translational Brain Research, State Key Laboratory of Medical Neurobiology, MOE Frontiers Center for Brain Science, Innovative Center for New Drug Development of Immune Inflammatory Diseases, Ministry of Education, Fudan University, Shanghai, 200040, China

<sup>b</sup> Department of Neurology, Zhongshan Hospital, Department of Laboratory Animal Science, MOE Frontiers Center for Brain Science, Fudan University, Shanghai, 200032, China

<sup>c</sup> Department of Medical Science, Medical College of Jinzhou Medical University, Jinzhou, Liaoning, 121010, China

<sup>d</sup> Department of Neurology, Shanghai Sixth People's Hospital Affiliated to Shanghai Jiao Tong University School of Medicine, Shanghai, 200233, China

<sup>e</sup> Shanghai Key Laboratory of Psychotic Disorders, Shanghai Mental Health Center, Shanghai Jiao Tong University School of Medicine, Shanghai, 201108, China

<sup>f</sup> Department of Neurology, Jinshan Hospital, Fudan University, Shanghai, 201508, China

## ARTICLE INFO

## Keywords:

Alzheimer's disease  
N6-methyladenosine  
METTL3  
WTAP  
Microglia  
ALKBH5

## ABSTRACT

N6-methyladenosine (m6A) modification is a common RNA modification in the central nervous system and has been linked to various neurological disorders, including Alzheimer's disease (AD). However, the dynamic of mRNA m6A modification and m6A enzymes during the development of AD are not well understood. Therefore, this study examined the expression profiles of m6A and its enzymes in the development of AD. The results showed that changes in the expression levels of m6A regulatory factors occur in the early stages of AD, indicating a potential role for m6A modification in the onset of the disease. Additionally, the analysis of mRNA m6A expression profiles using m6A-seq revealed significant differences in m6A modification between AD and control brains. The genes with differential methylation were found to be enriched in GO and KEGG terms related to processes such as inflammation response, immune system processes. And the differently expressed genes (DEGs) are negatively associated with genes involved in microglia homeostasis, but positively associated with genes related to "disease-associated microglia" (DAM) associated genes. These findings suggest that dysregulation of mRNA m6A modification may contribute to the development of AD by affecting the function and gene expression of microglia.

## 1. Introduction

Alzheimer's disease (AD) is a neurodegenerative disorder in the central nervous system (CNS) that leads to dementia. It is the most

\* Corresponding author.

E-mail address: [yanxiarao@fudan.edu.cn](mailto:yanxiarao@fudan.edu.cn) (Y. Rao).

<sup>1</sup> These authors contribute equally to this work.

common cause of dementia in the elderly. The pathological changes in AD primarily involve the deposition of  $\beta$ -amyloid ( $A\beta$ ) to form plaques, the phosphorylation of tau protein and the formation of neurofibrillary tangles (NFTs), eventually leading to neuronal damage [1]. Environmental exposure and genetic susceptibility are risk factors for AD [2]. However, the heterogeneity pathologies of AD among individuals with similar or identical susceptibility genes suggests the involvement of epigenetics in the disease.

Epigenetics refers to the heritable phenotype changes that occur without alterations in the DNA sequence, differing from genetics, which involves changes in the nucleotide sequence. Epigenetics mechanisms include DNA or RNA modification, histone modification, chromatin remodeling, and non-coding RNA regulation. N6-methyladenosine (m6A) is a common methylation modification on mRNA, occurring at the sixth nitrogen atom of adenine [3]. This modification is dynamically reversible. The regulatory factors involved in m6A methylation modification include "Writers" (methyltransferases), "Erasers" (demethylases), and "Readers" (binding proteins) of m6A [4]. The primary components of methyltransferase complex (MACOM) are methyltransferase-like 3 (METTL3), methyltransferase-like 14 (METTL14), and Wilms tumor 1-associated protein (WTAP), which cooperate with each other to perform catalytic functions [5,6]. Demethylases include fat and obesity-associated protein (FTO) and ALKB homolog 5 (ALKBH5) [7,8], while m6A methylation binding proteins comprise various proteins containing YTH domains [9], heterogeneous nuclear ribonucleoproteins (hnRNPs) [10], and eukaryotic initiation factor 3 (eIF3) [11]. Miao et al. [12] found that m6A modification is not random, and its content is related to the length and number of exons, and the distance from neighboring genes. Recent studies have revealed that epigenetic modifications can affect CNS development and function, such as neurogenesis, axon growth, synaptic plasticity, circadian rhythm, cognitive function, and stress response [13–15]. Dysregulation gene expression patterns controlled by epigenetics may lead to autoimmune diseases, cancer, and various other diseases. Previous studies have demonstrated that m6A-related proteins are widely expressed in neurons and play roles in various processes, including neurogenesis, memory formation and consolidation, cerebellar development, and axon regeneration [16–18]. Moreover, m6A modification abnormalities have been found in various neurodegenerative diseases, including AD [19,20].

Notably, while many studies have reported changes in m6A in AD, including alterations in METTL3, METTL14, and FTO, the dynamics of m6A and m6A enzymes during AD development remain unclear [21,22]. To address this, we analyzed m6A methylation levels and m6A regulatory factors in brain tissues from 5xFAD transgenic mice during various stages of AD progression. Additionally, we investigate the association of m6A and m6A regulatory factors with  $A\beta$ . We also applied mRNA m6A methylation sequencing (MeRIP-seq or m6A-seq) technology to investigate the changes in m6A modification at the genome-wide level during the AD process. These findings may offer a new perspective for understanding the potential role of m6A modification in AD pathogenesis and identifying new therapeutic targets for AD treatment.

## 2. Materials and methods

### 2.1. Animals

5xFAD (B6.Cg-Tg(APPswFLLon, PSEN1M146L, L286V, 6799Vas/Mmjax, Stock No: 008730) mice was purchased from The Jackson laboratory. They were used in this study along with their wild-type littermates at the ages of 3, 6, and 9 months. The mice were housed under a 12-h light/dark cycle and kept at a constant temperature of 22–24 °C. Food and water were provided ad libitum.

### 2.2. Tissue preparation for RNA extraction and immunohistochemistry

To prepare brain tissue for analysis, mice were anesthetized and perfused with either 50 ml of cold 0.01 M PBS or 0.9% NaCl. The right hemisphere or hippocampal tissue were collected. These tissues were then flash-frozen in dry ice and stored at  $-80$  °C prior to cryosectioning. RNA samples were extracted following the manufacturer's protocol provide by Takara (cat.9767). The left hemisphere was postfixed in 4% paraformaldehyde (PFA) overnight and then dehydrated with 30% sucrose in 0.01 M PBS at 4 °C for 2–3 days. Finally, the tissues were embedded in optimal cutting temperature (OCT) compound and stored at  $-80$  °C before cryosectioning.

## 3. Quantification of the m6A modification

In this study, the m6A RNA Methylation Quantification Kit (Epigentek , cat.P-9005 ) was used to measure the m6A content in total RNA samples. In this assay, total RNA is bound to strip wells using a RNA high binding solution. m6A is then detected with specific capture and detection antibodies. The signal is subsequently enhanced and quantified colorimetrically by reading the absorbance at a wavelength of 450 nm using a microplate spectrophotometer. Each reaction contained a total of 300 ng of RNA. The RNA m6A relative quantification assay was performed according to the manufacturer's protocol.

### 3.1. Quantitative Real-time PCR

Genomic DNA was removed from the total RNA, and cDNA was rapidly synthesized using PrimeScript™ RT reagent Kit with gDNA Eraser (Takara, cat.RR047A). TB Green® Premix Ex Taq™ (Tli RNaseH Plus) (Takara, cat.RR420A) and a LightCycler480 System (Roche Diagnostics) were utilized for qRT-PCR. *Gapdh* was served as the internal control. The relative expression of the following genes, *Ythdf1*, *Ythdf2*, *Ythdf3*, *Ythdc1*, *Mettl3*, *Mettl14*, *Wtap*, *Fto* and *Alkbh5*, were calculated using the 2- $\Delta\Delta$ Ct method. Details of the primer sequences used in this study are provided in [Supplementary Table 6](#).

### 3.2. Immunohistochemistry

All tissues were frozen in the freezing microtome for 15 min before cryosectioning. Coronal sections of the brain were cut at a thickness of 30  $\mu\text{m}$  by Leica CM1950 cryostat and then rinsed by 0.01 M PBS for 3 times. Brain sections were then blocked and permeabilized with 0.01 M PBS containing 0.3% Triton X-100 and 4% normal donkey serum (NDS) for 2 h at room temperature (RT). Next, the samples were incubated with primary antibody diluted in PBST containing 1% NDS at 4 °C ON. After being rinsed by 0.01 M PBS, 3 times, 10 min each, the sections were incubated with secondary antibody for 2 h at RT, together with 4',6-diamidino-2-phenylindole (DAPI, 1:1000). Following this, sections were rinsed by 0.01 M PBS for 3 times, mounted in anti-fade mounting medium, and the edges of the cover glass with nail enamel.

Primary antibodies included the following: Rabbit anti-METTL14 (sigma, cat.HPA038002, 1:500); Rabbit anti-YTHDF3 (Proteintech, cat.25537-1-AP, 1:500); Rabbit anti-ALKBH5 (Millipore, cat.ABE547, 1:500); Goat anti-IBA1 (Abcam, cat. ab5076, 1:500); Goat anti-Olig2 (Biotechne, cat.AF2418-SP, 1:500); Rabbit anti-YTHDF1 (Proteintech, cat.17479-1-AP, 1:500); Rabbit anti-YTHDF2 (Proteintech, cat.24744-1-AP, 1:500); Rabbit anti-WTAP (Proteintech, cat.10200-1-AP, 1:500); Rabbit anti-m6A (synaptic systems, cat.202003, 1:500); Rabbit anti-METTL3 (Abcam, cat.ab195352, 1:500); Mouse anti- $\beta$ -Amyloid (Biolegend, cat.803014, 1:2000); Mouse anti-NeuN (Abcam, cat.ab104224, 1:1000); Mouse anti-GFAP (Sigma, cat.G3893, 1:500); Rabbit anti-S100 $\beta$  (Sigma, cat. HPA015768, 1:500). Secondary antibodies included the following: AlexaFluor-488-, AlexaFluor-555-, or AlexaFluor-647-conjugated secondary antibodies against goat, rabbit, mouse (Invitrogen, 1:1000) antibodies.

### 3.3. Images acquisition and processing

Confocal images of fluorescent specimens were captured using NIKON A2 and Olympus FV3000 with objective lenses of 20 $\times$  (NA 0.75), 40 $\times$  (NA 1.30) or 60 $\times$  (NA 1.40). Z-stack images were taken and later processed for maximal intensity projection using Image J. For scanning entire coronal sections of the brain, either the Olympus VS120 or VS200 systems were employed. Images were saved in TIFF format using OlyVIA software. Adjustments for brightness and contrast were made within Image J as needed.

To assess the relative expression levels of the target protein, the protein fluorescence intensity for the target protein is obtained by subtracting the background fluorescence from total fluorescence emitted by the protein of interest. The value is referred to as the mean fluorescence intensity (MFI).

### 3.4. Western blot

Western blot analysis was performed according to established protocols. In brief, fresh brain tissue was lysed using RIPA buffer supplemented with 1 $\times$  proteinase inhibitor cocktail (Thermo Fisher). Next, the concentration of total protein was quantified through the BCA protein assay kit (Thermo Fisher). For electrophoresis, 25  $\mu\text{g}$  of total protein extract was loaded onto a 10% SDS-PAGE gel and then electrotransferred onto a PVDF membrane (Millipore). Primary antibodies used for target protein included the following: Mouse anti-FTO (Abcam, cat.ab92821, 1:1000 dilution), Rabbit anti-METTL14 (sigma, cat. HPA038002, 1:1000 dilution), Rabbit anti-YTHDF3 (Proteintech, cat.25537-1-AP 1:500 dilution), Rabbit anti-ALKBH5 (Millipore, cat.ABE547 1:1000 dilution), Rabbit anti-YTHDF1 (Proteintech, cat.17479-1-AP 1:1000 dilution), Rabbit anti-YTHDF2 (Proteintech, cat.24744-1-AP 1:5000 dilution), Rabbit anti-WTAP (Proteintech, cat.10200-1-AP 1:500 dilution), Rabbit anti-METTL3 (Abcam, cat.ab195352 1:1000 dilution), Mouse anti-GAPDH (Proteintech, cat.60004-1-Ig 1:20000 dilution). GAPDH was used as internal control. Following primary antibody incubation, membranes were treated with HRP-linked horse anti-mouse/rabbit IgG secondary antibodies (CST, cat.7076S/CST, cat.7074S) at a 1:2000 dilution. Target blots were detected using Enhanced ECL Chemiluminescent Substrate Kit (Yeasen Biotechnology, cat.36222ES60) and visualized by Touch Imager XLi (e-Blot) digital image scanner. For visualization, scanned images were adjusted for brightness and contrast to ensure optimal display. For the quantification of target protein, analysis was conducted using Image J. All data were represented as mean  $\pm$  SD. Statistical analysis was performed using GraphPad (v.9 Prism) with multiple unpaired t tests.

### 3.5. Magnetic-activated cell sorting (MACS)

Microglial cells were isolated from brains of 9-month-old C57BL/6J and 5x*FAD* mouse brain using CD11b-based MACS approach, as previously described by Xu et al. [23]. Briefly, mouse brains were dissociated using the gentleMACS Dissociators with a digestion buffer consisting of 8U/mL papain and 125U/mL DNase I. Myelin debris were then removed using 30% Percoll density gradient centrifugation. The resulting cell pellets were then rinsed once with 0.01 M DPBS containing 0.5% BSA. Next, the cells were incubated with human anti-mouse CD11b magnetic beads (Miltenyi, cat.130-042-401) at a 10% concentration for 30 min at 4 °C. CD11b-positive microglia were then selectively enriched and purified by passing the cells suspension through the LS column (Miltenyi, cat.130-042-401), which was attached to the QuadroMACS separator (Miltenyi, cat.130-091-051). These isolated and purified microglial cells were subsequently used for the subsequent qPCR analysis.

### 3.6. MeRIP-seq

Total RNA was isolated and purified using TRIzol reagent (Invitrogen) following the manufacturer's instructions. The quantity and purity of RNA from each sample were quantified using NanoDrop ND-1000 (NanoDrop), and RNA integrity was assessed using a Bioanalyzer 2100 (Agilent). Poly (A) RNA was purified from 50  $\mu\text{g}$  total RNA using Dynabeads Oligo (dT) 25–61005 (Thermo Fisher) in

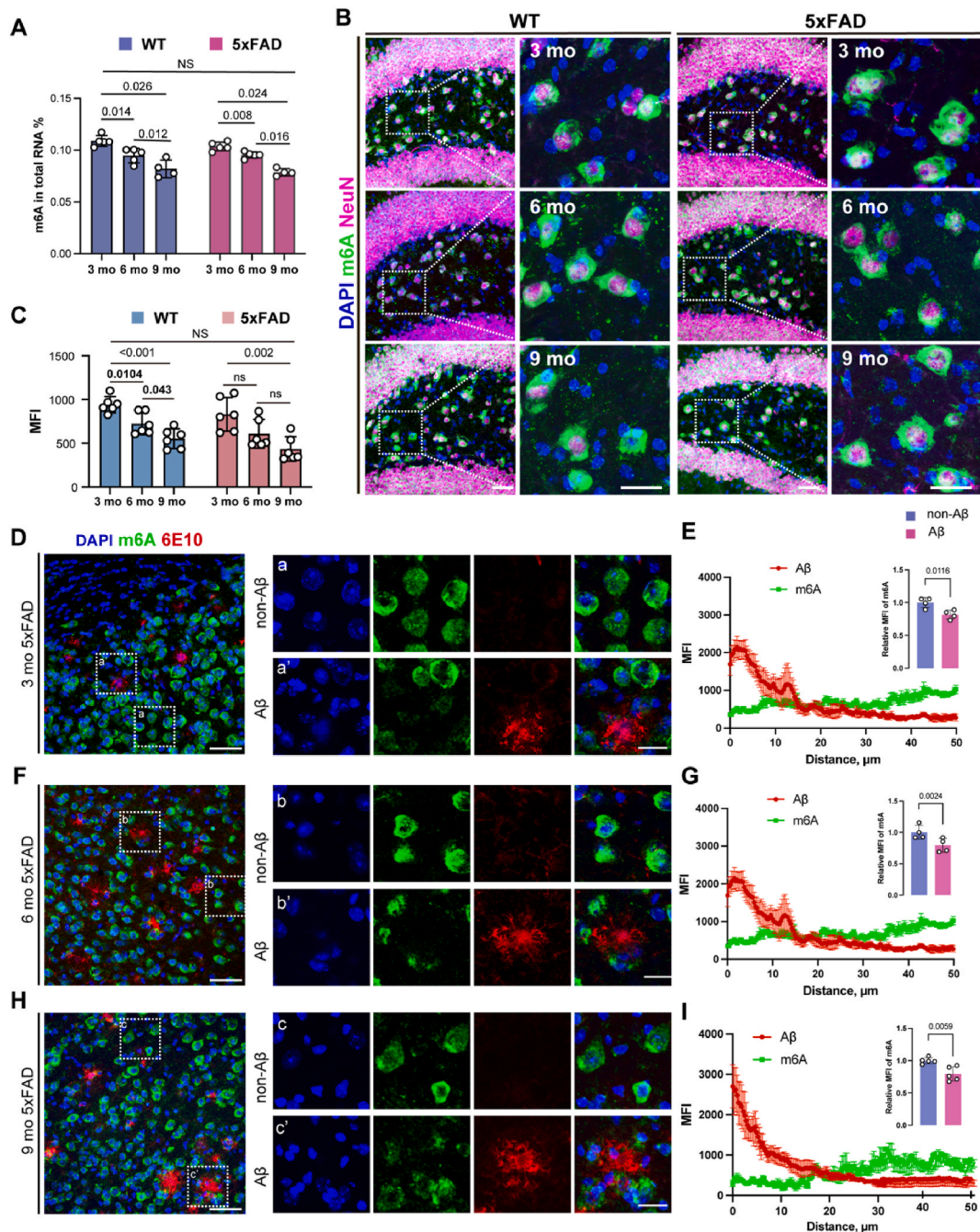


**Fig. 1.** Decline in m6A methylation levels in relation to A $\beta$  plaques in 5xFAD brain. **(A)** Quantitative analysis of m6A methylation in the hippocampus of 3, 6 and 9-month-old mice, showed a significant decrease in m6A levels when the mice aged. **(B)** Representative confocal images showing the co-staining of m6A (green) and neuron marker (purple) in the hippocampus of 5xFAD and age-matched WT mice. Included are zoom in views of these selected regions. **(C)** Bar chart presenting the mean fluorescent intensity (MFI) of m6A expression in NEUN-positive cells within the hippocampus from 5xFAD and age-matched WT mice. **(D, F and H)** Representative images showing m6A and A $\beta$  expression in the cortex in of 5xFAD mice at 3-month (D), 6-month (F) and 9-month (H). a, a', b, b', c and c' are zoom in views of these selected regions. **(E, G and I)** Line charts representing the distribution of both m6A and A $\beta$  MFI across different ages. Accompanying bar charts indicating a reduction in m6A expression levels in regions with high A $\beta$  intensity. 50  $\mu$ m in the main images, 20  $\mu$ m in the zoom-in views.

two rounds of purification. This poly(A) RNA was then fragmented into small pieces using Magnesium RNA Fragmentation Module (NEB, cat.e6150) under 86 °C for 7 min. The fragmented RNA was incubated with m6A-specific antibody (Synaptic Systems, cat. 202003) in IP buffer (50 mM Tris-HCl, 750 mM NaCl and 0.5% Igepal CA-630) for 2 h at 4 °C. The IP RNA was reverse-transcribed to cDNA by Superscript™ II Reverse Transcriptase (Invitrogen, cat. 1896649), followed by the synthesis of U-labeled second-stranded DNAs using *E. coli* DNA polymerase I (NEB, cat. m0209), RNase H (NEB, cat. m0297) and dUTP Solution (Thermo Fisher, cat. R0133). An A-base was added to the blunt ends of each strand, preparing them for ligation to indexed adapters. After ligating dual-index adapters, size selection was performed with AMPureXP beads. The U-labeled second-stranded DNAs were treated with a heat-labile UDG enzyme (NEB, cat. m0280), and the ligated products were amplified with PCR under specified conditions. At last, the cDNA library derived from both m6A-bound RNA and input RNA were subjected to paired-end sequencing (PE150) on an Illumina Novaseq™ 6000 platform, following the vendor's recommendations.

### 3.7. Bulk RNA-seq

The whole brain RNA were collected from 5xFAD and WT mice. The RNA integrity was evaluated using Agilent 2100 Bioanalyzer. Samples with an RNA Integrity Number (RIN)  $\geq 7$  were used for library preparation. Next, RNA libraries were prepared using the Illumina TruSeq preparation kit following the manufacturer's protocol. RNA was fragmented and then reverse transcribed into cDNA. Next, the sequencing adaptors were ligated and the library was amplified using PCR. At last, sequencing was performed on an Illumina Novaseq™ 6000 platform.

### 3.8. MeRIP-seq and RNA-seq data analysis

The quality of MeRIP-seq and RNA-seq data were evaluated using FastQC and RseQC. Low-quality reads and adaptor-containing reads were removed using fastp (v0.19.4). Mapping to the mm10 reference genome was accomplished using HISAT2 (v2.0.4). Peak calling and differential peak analysis were conducted in R (v4.2.2) using the exomePeak package (v2.16.0) and peak annotations were generated with ANNOVAR. MEME and HOMER (v4.10) were employed for both de novo and known motif discovery, and for assessing motif localization relative to peak summits. Transcript and gene expression levels in input libraries were determined using StringTie (v2.1.2), calculating FPKM values. Differential analysis based on the FPKM matrix was conducted using edgeR (v3.40.2) with quasi-likelihood (QL) F-tests. Genes showing an absolute  $\log_2(\text{fold change})$  greater than  $\log_2(1.5)$  and a p-value less than 0.05 were considered as significant differentially expressed genes (DEGs). Volcano plots were created using the EnhancedVolcano package (v1.16.0). GO and KEGG pathway analyses were conducted using the enrichGO and enrichKEGG functions of the clusterProfiler package (v4.6.2), with categories having an FDR of 0.05 or lower considered significantly enriched. These results were visualized using.

### 3.9. Statistical analysis

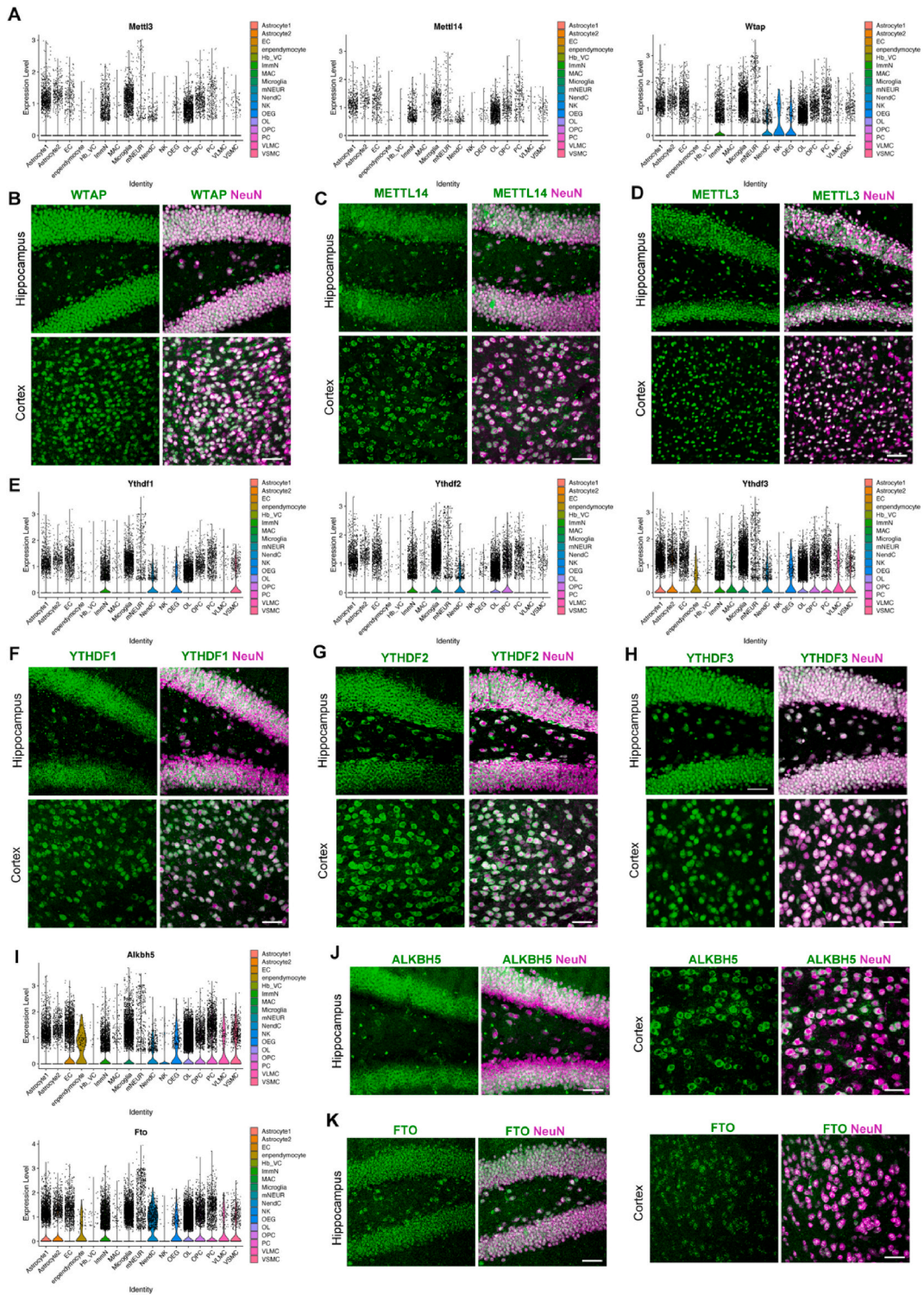
Statistical analysis was performed using GraphPad Prism (Version 9.0, La Jolla, USA). Each data point represented the average statistical result from three sections in different regions of the brain. Results were determined independently in a double-blind manner. If not otherwise specified, all data were shown as mean  $\pm$  standard deviation (SD). Data from multiple groups were evaluated statistically by one-way analysis of variance (ANOVA) with Holm-Sidak's multiple comparisons test (post hoc). Student's t-test was used for comparison between the two groups. Statistical significance was set as  $P < 0.05$ .

## 4. Results

### 4.1. A $\beta$ plaque accumulation is link to mRNA m6A modification

To investigate the changes in mRNA m6A levels during the progression of AD, we performed m6A detection in the hippocampal from 5xFAD and age-matched wild-type (WT) mice. The 5xFAD mouse begins to express a significant amount of A $\beta$ 42 at 2-month of age, leading to the development of pathological features such as amyloid-like protein accumulation and glial hyperplasia [24]. These mice exhibit a deterioration in learning and memory at the age of 6 months and neuronal apoptosis at the age of 9 months [24]. Therefore, we analyzed the m6A level at three time points, including 3-month (3 mo), 6-month (6 mo), and 9-month (9 mo). We observed a gradual decrease in m6A levels in both 5xFAD and WT mice as they aged (Fig. 1A). However, there was no significant difference in total m6A levels between 5xFAD and WT mice at these timepoints (Fig. 1A). We then investigated the expression profiles of m6A in neuron, microglia, oligodendrocytes, and astrocytes during AD progression by co-staining cell-specific markers with m6A (Fig. 1B and sFig.1). We found that m6A was more highly expressed in neurons than glial cells in the adult mouse brain (sFig.1). However, there were no significant differences in total m6A expression in neuron between AD and control groups across aging (Fig. 1B and C).

The accumulation of A $\beta$  plays a central role in the pathogenesis of AD, which contributes to neuronal dysfunction and neurodegeneration. Several mechanisms have been proposed to explain the impact of A $\beta$  on neuronal dysfunction, including synaptic loss, oxidative stress and inflammation, mitochondrial dysfunction, neuronal death and tau hyper phosphorylation [25,26]. However, the impact of A $\beta$  aggregation on mRNA m6A modification remains elusive. To investigate this, we examine the distribution of A $\beta$  plaques and m6A profiles using immunofluorescence (Fig. 1D–I). In our analysis, the center of an A $\beta$  plaque was established as the reference



(caption on next page)

**Fig. 2.** m6A regulatory factors are highly expressed in neurons both in the cortex and hippocampus. (A) scRNA-seq data from the whole brain of adult mouse suggesting the m6A “writers” (*Mettl3*, *Mettl14* and *Wtap*) both expressed in neurons and glial cells (B–D) Double labeling m6A “writers” (METTL3/14, WTAP) in conjunction with NeuN, a neuronal marker in the hippocampus and cerebral cortex of adult WT brains at 3 months of age. (E) scRNA-seq data presenting the expression patterns of m6A “readers” *Ythdf1*, *Ythdf2* and *Ythdf3* in various brain cells. (F–H) Co-expression analysis of m6A “readers” (YTHDF1-3) with NEUN in hippocampal and cortical tissues demonstrating their cellular localization in these regions. (I) scRNA-seq data showing the expression patterns of m6A “erasers” (*Alkbh5* and *Fto*) in different cell types within the mouse brain. (J, K) Representative confocal images displaying the co-staining of ALKBH5 and FTO with NEUN in the mouse brain, highlight co-localization of these m6A “erasers” in neurons. Scale bar: 50  $\mu$ m for all images.

origin. From this central point, eight radial lines were constructed, extending outward through the plaque. Along each of these radial axes, the fluorescence intensities of both A $\beta$  and m6A were quantitatively. Next, the value of the intensity were averaged. The region where the A $\beta$  fluorescence intensity over a baseline level was manually defined as the ‘peri-plaque region’ or the area surrounding the A $\beta$  plaque. We quantified the fluorescence intensity of m6A around A $\beta$  and non-A $\beta$  regions. The results showed that the levels of m6A surrounding A $\beta$  plaques were significantly lower compared to those in non-A $\beta$  region, as early as 3 months of age (Fig. 1D and E).

#### 4.2. Profiles the m6A enzymes expression in the adult brain

The observed reduction in m6A levels surrounding A $\beta$  plaques suggested a potential link between A $\beta$  plaques formation and alterations in mRNA m6A modification during AD development. To further explore this relationship, We examined the expression features of m6A readers (YTHDF1, YTHDF2, YTHDF3) (Fig. 2E–H), writers (METTL3, METTL14, and WTAP) (Fig. 2A–D), and erasers (ALKBH5 and FTO) (Fig. 2I–K) in normal brain. Firstly, we assessed the expression of these m6A enzymes in neurons and glial cells using whole brain scRNA-seq data (GEO with accession code GSE207948) from adult mouse brain, building on our previous findings [27]. We observed that *Ythdf1*~3, *Ythdc1*, *Igf2bp3*, *Mettl3*, *Mettl14*, *Wtap*, *Alkbh5*, and *Fto* were widely expressed in 16 populations identified, except for hemoglobin-expressing vascular cells (Hb-VC) (Fig. 2A, E and 2I, sFig2). All regulatory factors were highly enriched in immature neuron (ImmN) but not in mature neurons (mNEUR) as shown in Supplementary Fig. 2. Additionally, *Ythdf2*, *Ythdf3*, *Wtap*, *Alkbh5* and *Fto* were highly expressed in glial cells, including astrocytes, oligodendrocyte precursor cells, oligodendrocytes, and microglia (Fig. 2E and 2I, and sFig.2).

Next, we delved deeper into the cellular localization of these regulatory factors in the adult mouse brain using immunofluorescence. The m6A regulatory factors were co-stained with markers for neuronal and glia cells. In these regulatory factors, WTAP (Fig. 3G and H), METTL3 (Fig. 3I and J), and FTO (Fig. 3M and N) were primarily localized in the nucleus of both neurons and glial cells. Conversely, others exhibited expression in both nucleus and cytoplasm, as detailed in Figs. 2 and 3. Contrary to observations from scRNA-sequencing, we found that these m6A regulatory factors were more broadly and intensely expressed in mature neurons within the hippocampus and cortex, as compared to their expression in glial cells in the steady state (Fig. 3B, D, 3F, 3J and 3P). Also, there is a notable deviation from scRNA-sequencing data, which suggested that factors, such as YTHDF1, YTHDF2, YTHDF3, METTL14, and ALKBH5 were highly enriched in microglia and oligodendrocytes (Fig. 2E, A and 2I). In our observations, these regulatory factors were detected only in a subset of microglia and oligodendrocytes (Fig. 3A, C, 3E, 3I, and 3O). Their expression levels in these cells were relatively low compared to those in neurons (Fig. 2 and sFig.3). The discrepancies between the immunofluorescence staining and scRNA-sequencing data might stem from the nature of the isolated whole-brain cells used in analysis. If these cells do not cover all cell types presented in the brain, it could lead to an incomplete picture of the expression patterns of these regulatory factors. Additionally, the immunofluorescence studies primarily focused on the hippocampus and cortex, potentially neglecting the expression of these factors in other brain regions.

#### 4.3. Dynamic changes of m6A-related regulatory factors in the progression of Alzheimer’s disease

Next, we investigated the alterations in m6A-related regulatory factors at the RNA level during different stages of AD progression. Firstly, we analyzed previous published mouse bulk RNA-seq data (GEO with accession code GSE168137), focusing on the dynamic changes of m6A enzymes during the development of AD [28]. We found that *Wtap* exhibited significant downregulation during the early stage of AD (4-month-old), whereas *Ythdc1*, *Ythdf3*, and *Fto* showed significant downregulation in expression in the later stages of AD (18-month-old) compared to control samples (sFig. 4D–G and I). We additionally conducted a comparative analysis of these regulatory factors detected in human AD brain (GEO with accession code GSE236562) (Fig. 4F) [29]. Bulk RNA data from this small cohort of AD patients indicated a trend of altered expression of multiple m6A regulatory factors. Furthermore, significant regional variability was observed in the expression of these m6A regulatory factors (Fig. 4F) [29].

In this study, we systematically analyzed the genes expression levels of key m6A regulatory factors in the hippocampus of adult mice specifically at 3, 6, and 9 months of age (Fig. 4A–D and Supplementary Table 1). At 3-month old, the expression level of *Mettl3*, *Wtap* and *Alkbh5* decreased by approximately 10% and exhibited significant difference in 5xFAD mice, compared to wild type mice (Fig. 4B). YTHDF2 facilitates the degradation of mRNA by directing m6A-modified RNA to sites of mRNA decay. While, YTHDF3 plays a dual role in the cytoplasm, which enhances translation in coordination with YTHDF1 and promotes degradation in conjunction with YTHDF2 [30]. Previous studies have highlighted the role of YTHDF2 in regulating hippocampal dentate gyrus-dependent learning and memory [31]. Furthermore, In the context of AD and asymptomatic mild cognitive impairment (MCI), there is a significant positive correlation between the abundance of YTHDF3 in the prefrontal cortex and higher cognitive performance [32]. Notably, at 6-month

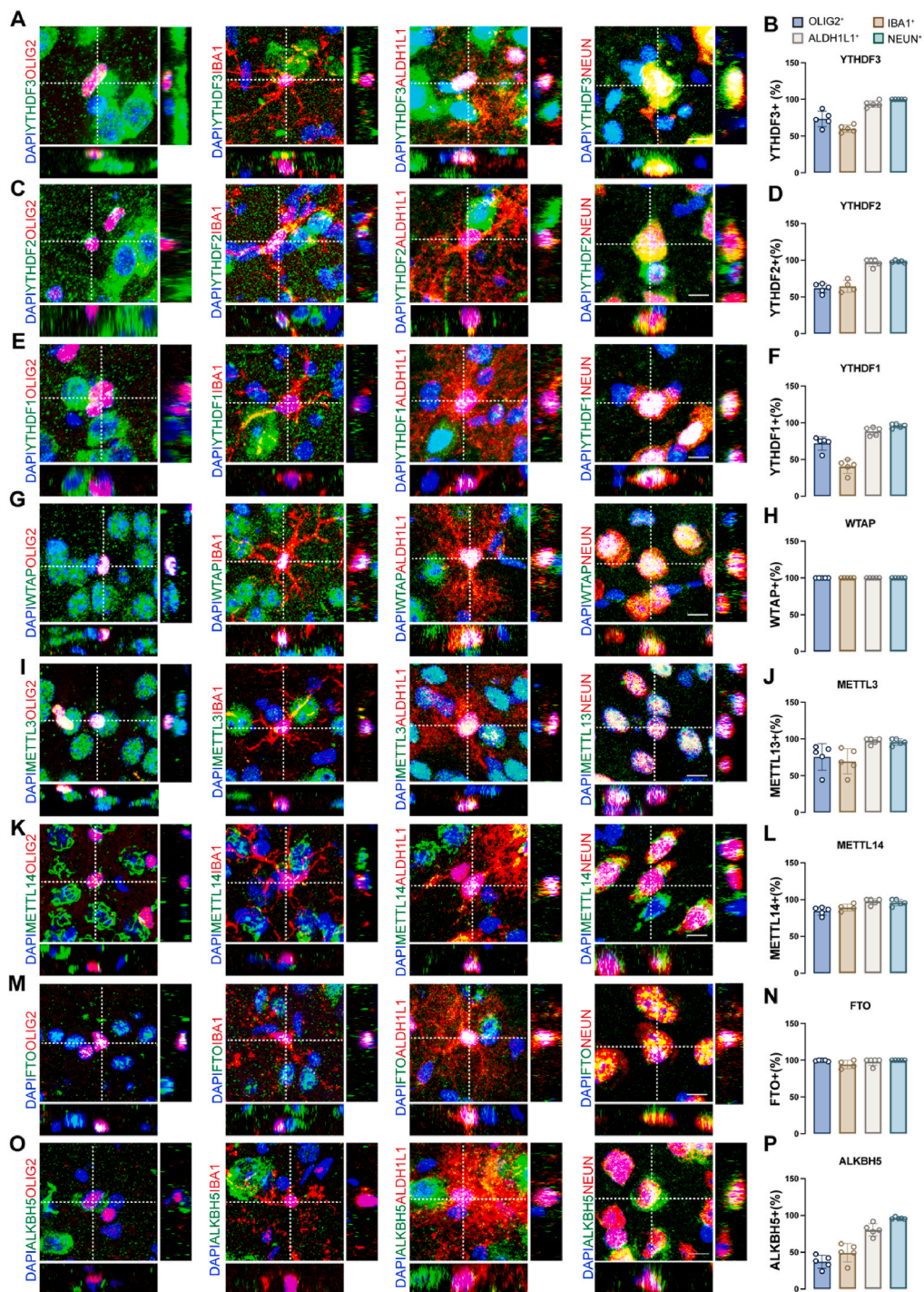


**Fig. 3.** m6A-related factors are expressed both in glial cells and neurons. (A) Representative confocal images showing the orthogonal view of YTHDF3 (green) in relation to glia cell markers IBA1, OLIG2 and ALDH1L1 (red), NEUN (red) and DAPI in the cortex in adult brain. (B) Bar chart showing the distribution of YTHDF3 in OLIG2, IBA1, ALDH1L1 and NEUN positive cells. (C) Representative confocal images suggesting YTHDF2 (green) are highly expressed predominantly in the perinuclear area of both glial and neuron cells. (D) Bar chart showing the distribution of YTHDF2 in OLIG2, IBA1, ALDH1L1 and NEUN positive cells. (E) Orthogonal view of YTHDF1 (green) indicating YTHDF1 expressed in both nuclei and perinuclear areas in both glial and neuron cells. (F) Bar chart demonstrating the distribution of YTHDF1 in OLIG2, IBA1, ALDH1L1 and NEUN positive cells. (G) Orthogonal view of WTAP (green) indicating its nuclei expression in both glial and neuron cells. (H) Bar chart showing the distribution of WTAP in OLIG2, IBA1, ALDH1L1 and NEUN positive cells. (I) Representative confocal images suggesting nuclear expression of METTL3 (green) in both glial and neuron cells. (J) Bar chart illustrating the distribution of METTL3 in OLIG2, IBA1, ALDH1L1 and NEUN positive cells. (K) Representative confocal images suggesting METTL14 (green) are primarily expressed in the perinuclear region in astrocytes and neuron cells. (L) Bar chart

showing the distribution of METTL14 in OLIG2, IBA1, ALDH1L1 and NEUN positive cells. (M) Orthogonal view of FTO (green) indicating FTO are expressed in nuclei in both glial and neuron cells. (N) Bar chart showing the distribution of FTO in OLIG2, IBA1, ALDH1L1 and NEUN positive cells. (O) Orthogonal view of ALKBH5 (green) indicating ALKBH5 are mainly expressed in peri-nuclei in astrocytes and neuron cells. (P) Bar chart showing the distribution of ALKBH5 in OLIG2, IBA1, ALDH1L1 and NEUN positive cells. Bar chart is 10  $\mu\text{m}$ .

old, we observed a significant downregulation in the expression of *Ythdf2* and *Ythdf3* in 5xFAD mice (Fig. 4C). Unexpectedly, at 9 months of age, there were no significant differences in gene expression between the 5xFAD and WT (Fig. 4D). The changes in *WTAP* that we observed at 3 months of age were consistent with the previous sequencing data, indicating that alterations in m6A enzymes indeed occur early on during AD development (Fig. 4E).

Additionally, we investigated the overall protein expression levels of m6A regulatory factors throughout the brain (Fig. 4G–L). In early-stage AD, a noticeable decrease in the expression of m6A readers, specifically YTHDF3 and YTHDF2 proteins, was observed in AD brains, as evidenced by Western blot (WB) analysis (Fig. 4G and J, and sFig.5A, 5B). This decline was especially pronounced for YTHDF3 in 9-month-old AD brains, as confirmed by both WB and immunofluorescence (Fig. 4I and L, sFig.5C). Notably, we observed that the protein expression patterns were distinct from the gene expression profiles identified in the hippocampal region. Previous research has shown that m6A regulatory factors exhibit varying expression levels in different brain regions in relation to specific diseases. For instance, in Parkinson's disease (PD), the expression pattern of YTHDF3 is notably diverse. In human PD samples, YTHDF3 expression was found to be reduced in the cingulate gyrus and frontal cortex. Conversely, a significant increase in YTHDF3 expression was observed in the cerebellum of PD patients. Moreover, a global increase in YTHDF3 immunoreactivity was evident in PD, highlighting its potentially complex role in the disease [32].

#### 4.4. The expression profile of *METTL3* and *WTAP* is closely associated with the deposition of $A\beta$ in the hippocampus

Although no significant reductions were observed in the protein levels of m6A writers in the entire brain, the downregulation of m6A writer genes (*Mettl3* and *Wtap*) in the hippocampus warrants further investigation. As previous studies have demonstrated that dysregulation of *WTAP* and *METTL3* is dysregulated in the brains of AD patients and in animal models of AD [21]. We conducted an in-depth examination of these proteins during AD progression (Fig. 5A). There was no significant difference in the total expression of *METTL3* and *WTAP* in the cortex in the AD brain compared to WT at different stages of AD, from 1 month to 9 months of age (sFig.6). However, the expression pattern of *WTAP* and *METTL3* were associated with the deposition of  $A\beta$ . The reduction of *METTL3* began as early as 3 months old (Fig. 5B–G), whereas the decrease in *WTAP* expression started close to 6 months old (Fig. 5H–M). This implies that the decline in *METTL3* expression occurs earlier than *WTAP* during the development of AD (Fig. 5E, K and 5L).

#### 4.5. MeRIP-seq analysis of AD brain

To further understand RNA m6A modification alterations in AD, methylated RNA immunoprecipitation sequencing (MeRIP-seq) was conducted on the whole brain of 9-month-old 5xFAD and age-matched WT mice (Fig. 6A). The m6A peaks in the genome were annotated, which signify genomic regions undergoing m6A modifications. This analysis identified 11,664 m6A modification sites in the WT group and 11573 in the 5xFAD group. There was a substantial overlap of 10,884 modification sites between the two groups (Fig. 6C–Supplementary Table 2). The exomePeak package was used for genome-wide peak scanning. We observed that m6A peaks predominantly localized to the coding sequence (CDS), 3' untranslated region (3'UTR), and 5' untranslated region (5'UTR) in both the AD and WT groups (Fig. 6B). Next, the differential peaks between the two groups were analyzed, with an absolute fold change over 1.5, and P-value less than 0.05. We found that there were 607 upregulated and 645 downregulated m6A peaks in the 5xFAD brain, compared to control (Fig. 6D). The GO and KEGG pathway annotations suggested that differentially expressed m6A-modified genes found in 5xFAD were involved in process related to serine/threonine kinase activity, DNA damage, cellular senescence, apoptosis, and N-glycan biosynthesis (Fig. 6E and F, and Supplementary Table 3).

To investigate the relationship between m6A methylation and gene expression in the AD process, we performed RNA-seq on the two groups at the same age as well. The analysis of differentially expressed genes (DEGs) revealed that, compared to the WT group, 77 genes were significantly upregulated and 31 genes were significantly downregulated in the 5xFAD mouse brain (Fig. 7A). Subsequently, based on the results of differential genes and m6A peak data, a correlation analysis was performed to integrate transcription levels with m6A methylation (Fig. 7B). A four-quadrant plot was generated to visualize the relationship between changes in m6A methylation and gene expression. The hyper-up quadrant represented genes with both upregulated m6A peaks and increased gene expression. The hyper-down quadrant represented genes with upregulated m6A peaks but decreased gene expression. The hypo-up quadrant represented genes with downregulated m6A peaks but increased gene expression. The hypo-down quadrant represented genes with both downregulated m6A peaks and decreased gene expression. We identified 25 genes in the hyper-up quadrant (like *Clec7a*, *Mpeg1*, *H2q7*, *H2k1*), 14 genes in the hypo-down quadrant (such as *Pigh*, *Tomt*, *Zbed5*), 33 genes in the hyper-down quadrant (*Cap6*, *Cstad*, *Lsm2*, *Cradd*) and 31 genes in the hypo-up quadrant (*Ilr1*, *Gvin1*, *Ch25h*, *Ifit3*) (Fig. 7B and Supplementary Table 4).

Next, we performed GO term enrichment and KEGG analysis on the genes identified in the four quadrants. The results indicated that the genes with differential m6A peaks identified in the AD were enriched in biological processes such as leukocyte migration, regulation of IFN $\gamma$  production, VEGF production, and regulation of Th1 immune response (Fig. 7C). These processes are crucial for immune system function [33–35]. The KEGG analysis revealed that the genes with expression related to changes in m6A peak expression in the

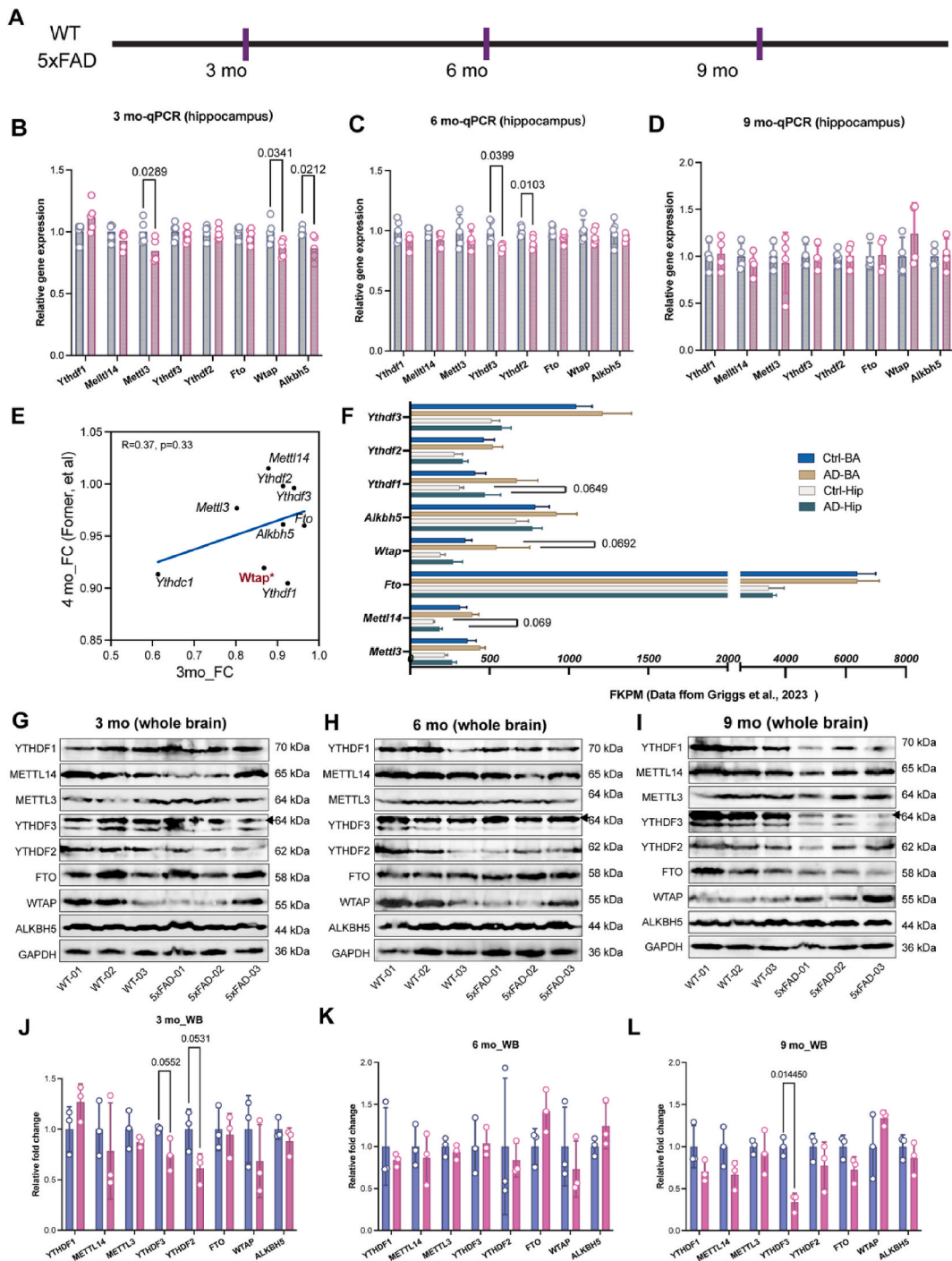


**Fig. 4.** Dynamic expression of m6A regulatory factors in the progression of AD (A) Schematic representation of the experimental design, indicating the time points for RT-qPCR and Western blot (WB) analysis at 3, 6, and 9 months of age. (B–D) Bar graphs showing the quantification of the relative expression level of m6A-related genes in the hippocampus of WT and 5xFAD mice.  $n = 5$  biological replicates for p value are provided in figures. (E) Correlation analysis between the fold change of m6A-related genes in 3-month-old versus 4-month-old mice, based on public data from GSE168137. (F) Bar graphs showing the expression of m6A-related genes in the hippocampus (Hip) and cortical basal ganglia (BA) from human AD patients and healthy controls, using data from Griggs et al., GSE236562. (G–I) Western blot (WB) analyses showing the protein expression levels of global m6A-related factors in the whole brain of 5xFAD and WT mice at 3, 6, and 9 months of age. (J–L) Bar graphs showing the quantification of m6A-related protein expression levels in 5xFAD and WT mice at 3, 6 and 9-month of age, as determined by WB analysis shown in G to I.

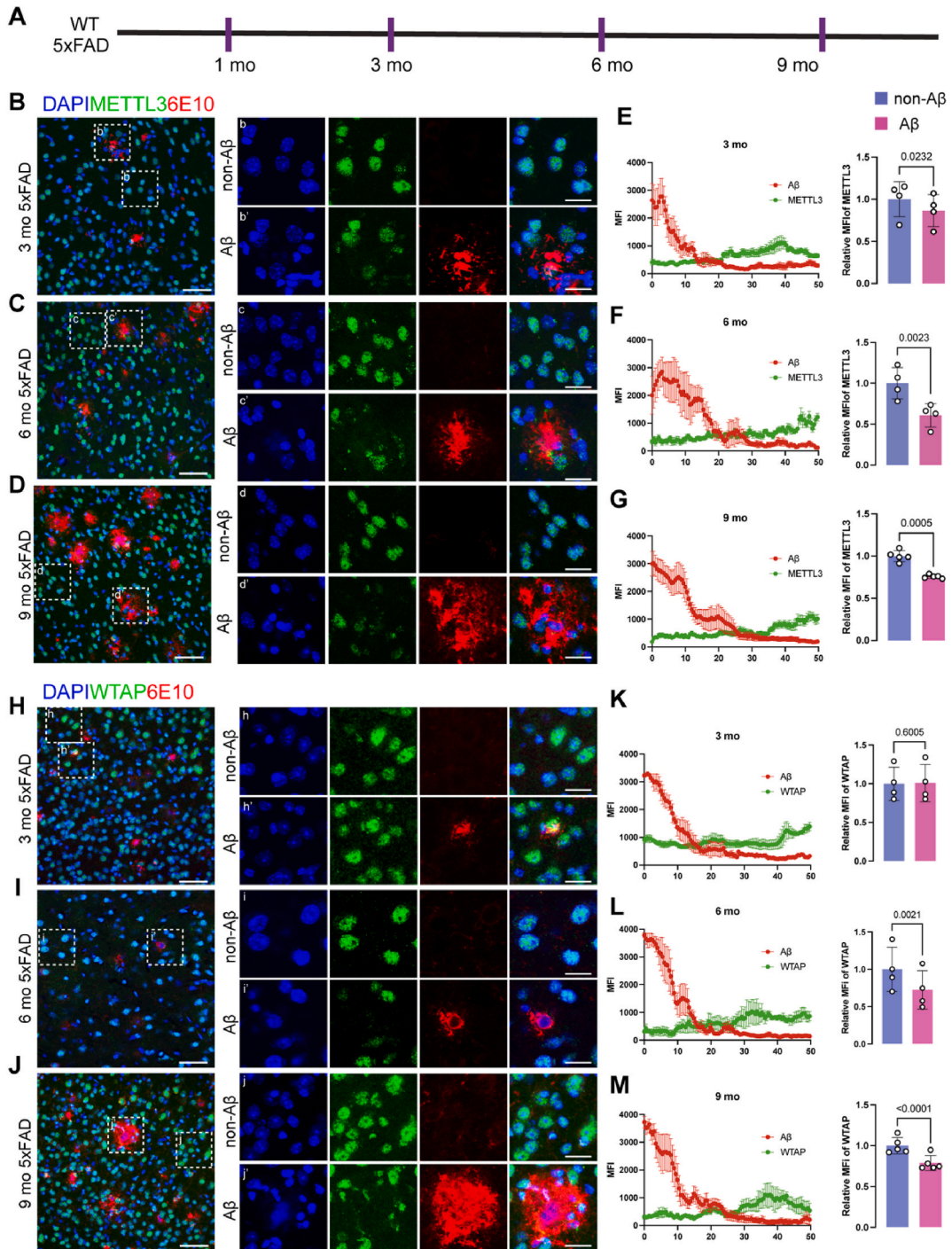


**Fig. 5.** Impact of A $\beta$  pathology on METTL3 and WTAP expression. (A) Schematic representation of the experimental timeline for data collection at 1, 3, 6, and 9 months of age. (B–D) Representative confocal images showing the expression of METTL3 (green) and A $\beta$  plaques labeled with 6E10 (red) at various ages in 5xFAD mice. DAPI staining (blue) indicates nuclei. Insets b, b', c, c', d and d' provide magnified views of selected areas. (E–G) Line graphs showing the distribution of MFI of METTL3 and A $\beta$ , accompanying with quantitative analysis of METTL3 fluorescence intensity in regions with and without A $\beta$  plaques in 3, 6, and 9-month-old 5xFAD mice brains. (H–J) Representative confocal images showing co-staining of WTAP (green) and A $\beta$  plaques labeled with 6E10 (red) across different ages in 5xFAD mice. DAPI staining (blue) indicates nuclei. (K–M) Line charts showing the MFI profiles of WTAP and A $\beta$ , along with bar charts showing the quantitative analysis of WTAP fluorescence intensity around A $\beta$  and non-A $\beta$  regions in 3, 6 and 9-month-old 5xFAD mice brains. 50  $\mu$ m for the main images, 20  $\mu$ m for the zoom-in views.

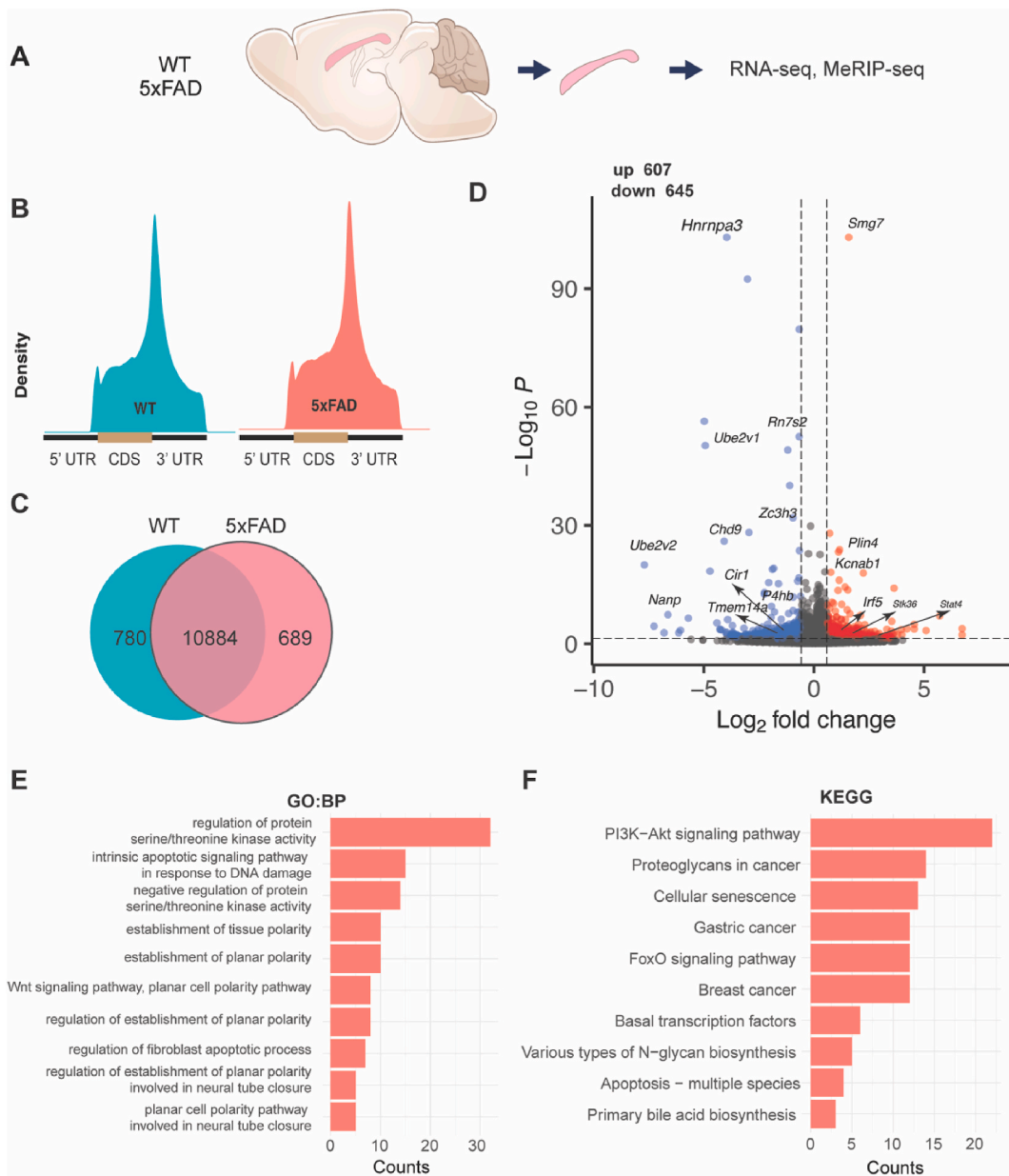


**Fig. 6.** MeRIP-seq reveals the alteration in the m6A modification patterns in AD mouse model. (A) Schematic diagram showing the experimental design. (B) Kernel density plots showing the distribution of average m6A peaks regions across all transcripts between WT and 5xFAD mice, highlighting differences in the 5' UTR, CDS, and 3' UTR. (C) Venn diagram showing the differences in identified m6A peaks between WT and 5xFAD mice, revealing shared and unique methylation sites. (D) Volcano plots showing mRNAs with significantly altered m6A peaks in 5xFAD, with upregulated peaks marked in red and downregulated peaks in blue. (E) Bar chart representing the top 10 enriched GO: biological process terms associated with genes exhibiting altered m6A peaks. (F) Bar chart displaying the top 10 enriched KEGG pathways with the greatest number of enriched genes.

AD group were mainly enriched in several key pathways, including neutrophil extracellular trap formation, cytokine-cytokine receptor interaction, steroid hormone biosynthesis, platelet activation, primary bile acid biosynthesis, and glycosaminoglycan degradation (Fig. 7D and Supplementary Table 5). These pathways have been implicated in the clearance of A $\beta$  plaques, regulation of innate immune response, regulation of neuroprotective, regulation of cerebral blood flow and lipid metabolism in the brain, respectively [36–39].

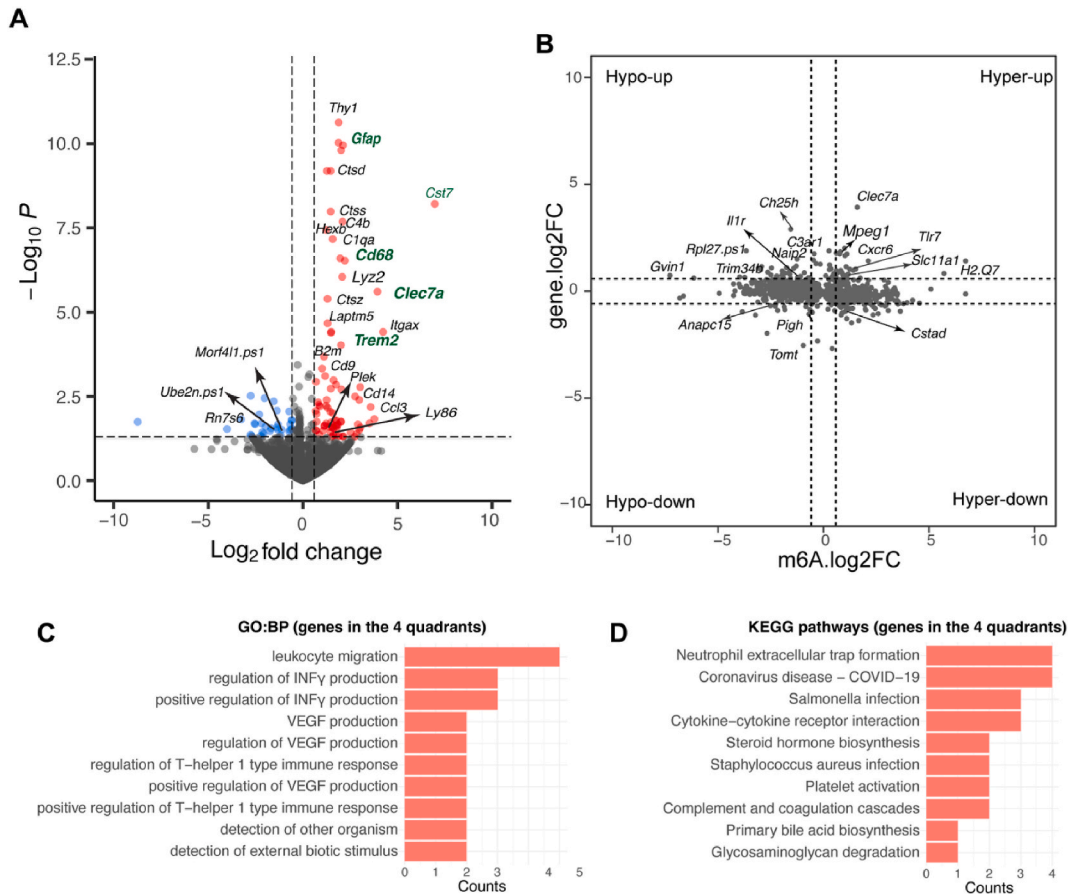


**Fig. 7.** Integrative analysis of gene expression and m6A methylation. (A) Volcano plots showing the differentially expressed genes identified in 5xFAD, with significant upregulations shown in red and downregulations in blue. (B) Four-quadrant plots categorizing genes by their m6A methylation ( $\log_2$  FC) and mRNA expression levels ( $\log_2$  FC), identifying hyper-up, hypo-down, hyper-down, and hypo-up gene sets. (C) Bar chart showing the top 10 GO biological process terms for genes in the four quadrants. (D) Bar chart depicting the top 10 KEGG pathways for the genes in the four quadrants.

#### 4.6. RNA m6A methylation and the correlation with microglia transcription

Given that most genes modified with m6A were associated with the innate immune response, we hypothesized that mRNA m6A methylation plays a role in regulation of microglial gene expression in response to AD pathogens. Microglia are crucial innate immune cells in the brain and are pivotal in the development of AD [40]. Specifically, the disease-associated microglia (DAM) represent a distinct subset of microglia that have been identified in the context of neurodegenerative diseases such as AD, and these cells show distinctive DAM signatures [41]. DEGs analysis between WT and 5xFAD mice identified 25 genes that previously reported DAM signature genes (*Cst7*, *Trem2*, *Ccl3*, *Cd74*) (Fig. 8A and B). We observed a positive correlation between m6A modification and these 25 DAM signature gene ( $R = 0.8092$ ,  $P < 0.0001$ ) (Fig. 8C). Differential m6A peaks were found to be accumulating in the coding regions of these genes, such as *Csf1*, *Ccl6*, *Mpeg1*, and *Cd68* (Fig. 8D). These findings suggested a significant association between m6A modifications and microglial activation in AD.

To this end, we further employed the MACS technique to isolate microglia from the brain of 9-month-old AD and WT mice. We then examined the expression levels of m6A and m6A regulatory factors (Fig. 8E). Our findings revealed an increased trend in m6A levels within microglia (Fig. 8F). Notably, there were significant upregulation in the expression of m6A readers (*Ythdf1*, *Ythdf2*, *Ythdf3*) and the eraser (*Alkbh5*) in microglia from 5xFAD (Fig. 8G). Further analysis revealed an upregulated expression of m6A eraser, ALKBH5 but not m6A readers in microglia surrounding A $\beta$  plaques within the hippocampal region (Fig. 8H and I). These observation a potential role of ALKBH5 in microglial responses to the accumulation of A $\beta$  plaques, highlighting a specific aspect of microglial involvement in AD pathology mediated by m6A modifications.

## 5. Discussion

RNA m6A methylation has been widely accepted for its association with cancer, such as breast cancer and lung cancer [42], but the

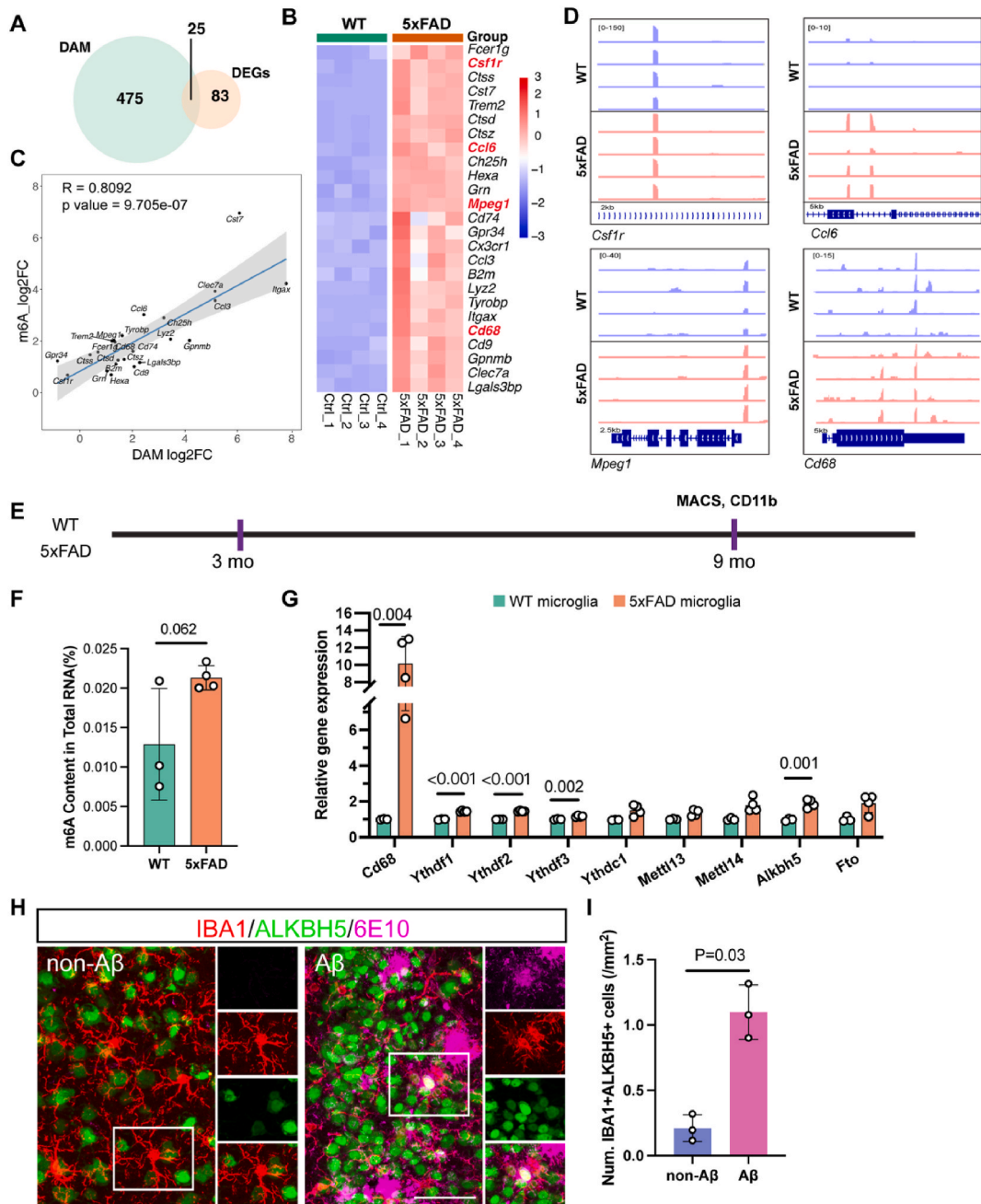


**Fig. 8.** Genes with altered m6A modification are associated to microglia in 5xFAD mice. (A) Venn diagrams showing genes identified as disease-associated microglia (DAM) signature genes and differentially expressed genes (DEGs) in 9-month old 5xFAD. (B) Heatmap showing the differential expression of 25 DAM signature genes in the brains of 9-month-old ADs. (C) Scatterplot showing the correlation between the log2 fold change of DAM and DEGs identified in 9-month old AD brains. (D) Genome browser tracks of *Csf1*, *Ccl6*, *Mpeg1* and *Cd68* suggesting regions of increased m6A modifications in AD brains. (E) Scheme diagram of the magnetic-activated cell sorting (MACS) method used to isolate microglia from 9-month-old AD and WT mice. (F) Quantification of total RNA m6A methylation levels within microglia. N = 3 or 4 biological replicates for each group. (G) Bar charts showing the relative expression levels of m6A-related genes in microglia isolated from WT and 5xFAD mice. (H) Immunofluorescence images showing IBA1 (red) and ALKBH5 (green) co-localization in regions with and without amyloid-beta (A $\beta$ ) plaques. Insets show zoomed-in areas of interest. Scale bar is 50  $\mu$ m. (I) Quantitative analysis of the number of IBA1 and ALKBH5 double positive cells around A $\beta$  region and non-A $\beta$  region.

relationship between RNA m6A methylation and CNS pathology remains largely unexplored. In this study, we focused on the dynamics of RNA m6A modification and m6A regulatory factors during the development of AD. Immunofluorescence results revealed that RNA m6A modification is relatively high in neurons, but low in glial cells. Also, most m6A regulatory factors are highly expressed in neurons

than those in glia cells. But the precise reason for the relative low level of m6A modification and m6A regulatory factors in glial cells is not fully understood. Overall, the total RNA m6A modification levels gradually decreases with age, with no significant difference between AD and age-matched controls. However, there was a decline in RNA m6A modification levels surrounding A $\beta$  plaques as early as 3-month old. We also observed alterations in the expression of m6A regulatory factors during AD development, suggesting a link between dysregulated RNA m6A modification and the onset of AD.

Previous studies also reported a significant upregulation of METTL3, and downregulation of RBM15B in the hippocampus of AD brains [43]. Additionally, Zhao et al. reported that METTL3 and METTL14 expression are significantly decreased in the brain tissue from patients with mild cognitive impairment, a precursor stage of AD [21], implying a role for RNA m6A modification in the early stage of AD. In the hippocampus regions, the reduction of m6A modification caused by *Mettl3* gene knockout results in cognitive and memory impairment, which are characteristics of AD [44]. This study also demonstrated that METTL3 is necessary for the maintenance of dendritic spine and synaptic integrity, as well as neuronal survival [44]. Another study showed that suppression of FTO demethylase could rescue METTL3 depletion-induced decreased m6A modification and neuronal deficit in AD [45]. Contrary to our observation of a gradually decreased m6A modification in the AD brain during AD development, another study found that the level of RNA m6A methylation is increased in the cortex and hippocampus of an AD mouse model (APP/PS1 transgenic mice) compared to control, and the expression level of METTL3 is upregulated while FTO is downregulated in AD mice [46]. The reason for this discrepancy may be attributed to the different AD mouse models used.

In our MeRIP-seq analysis of AD and WT, we discovered that the differentially methylated peaks were enriched in GO and KEGG terms related to biological processes such as inflammation response, immune system processes, signal transduction, positive regulation of lipid metabolism, and cytokine production. These findings suggest a link between m6A methylation and the regulation of microglia activation. Microglia are the innate immune cells in the CNS, which has a central role in the AD [47]. One study demonstrated that silencing of the m6A methyltransferase METTL14 lead to reduce expression of pro-inflammatory genes but increase expression of anti-inflammatory genes in microglia, suggesting that m6A methylation regulates microglial polarization and activation [48]. Another study found that METTL3 is upregulated in microglia activated by lipopolysaccharide (LPS) stimulation [49]. Inhibition of METTL3 decrease the expression of pro-inflammatory cytokines and chemokines in microglia [49]. Furthermore, another study found that RNA m6A methylation plays a critical role in the regulation of microglial phagocytosis [50]. Our observation suggested ALKBH5 is closely linked to microglia response to A $\beta$  accumulation. Thus, our finding suggested that mRNA m6A methylation plays a crucial role in the regulation of microglia function, and its dysregulation could contribute to the pathogenesis of AD.

### Ethics approval and consent to participate

All animal procedures adhered to the guidelines set by the Institutional Animal Care and Use Committee and were conducted in the Animal Facility of the Department of Laboratory Animal Science at Fudan University.

### Consent for publication

Not applicable.

### Availability of data and materials

MeRIP-seq data are available in the Genome Sequence Archive (GSA) with accession code CRA010646.

### Funding

This work was supported by by STI2030-Major Projects, China (2022ZD0207200) (Y.R.) and (2022ZD0204700) (B.P.), National Natural Foundation of China, China (32000678) (Y.R.), National Natural Science Foundation of China, China (32170958) (B.P.) Program of Shanghai Academic/Technology Research Leader, China (21XD1420400) (B.P.), Shanghai Pilot Program for Basic Research, China (21TQ014) (B.P.), The Innovative Research Team of High-Level Local University in Shanghai (B.P.), “Shuguang Program” supported by Shanghai Education Development Foundation, China and Shanghai Municipal Education Commission, China (22SG07) (B.P.)

### CRedit authorship contribution statement

**Shuai Gao:** Data curation. **Yuqing Wang:** Writing – original draft, Data curation. **Xiaoyu Li:** Software, Data curation. **Yuqing Liang:** Data curation. **Zhihao Jin:** Formal analysis. **Baozhi Yang:** Visualization, Methodology. **Ti-Fei Yuan:** Writing – review & editing. **Hengli Tian:** Writing – review & editing, Visualization. **Bo Peng:** Supervision, Funding acquisition. **Yanxia Rao:** Writing – original draft, Supervision, Funding acquisition.

### Declaration of competing interest

The authors declare the following financial interests/personal relationships which may be considered as potential competing interests:

## Acknowledgements

The authors express their gratitude and respect to all animals sacrificed in this study.

## Appendix A. Supplementary data

Supplementary data to this article can be found online at <https://doi.org/10.1016/j.heliyon.2024.e26911>.

## References

- [1] P. Scheltens, et al., Alzheimer's disease, *Lancet* (London, England) 397 (10284) (2021) 1577–1590.
- [2] W. Xu, et al., Meta-analysis of modifiable risk factors for Alzheimer's disease, *J. Neurol. Neurosurg. Psychiatry* 86 (12) (2015) 1299–1306.
- [3] Y. Fu, et al., Gene expression regulation mediated through reversible m<sup>6</sup>A RNA methylation, *Nat. Rev. Genet.* 15 (5) (2014) 293–306.
- [4] X. Jiang, et al., The role of m<sup>6</sup>A modification in the biological functions and diseases, *Signal Transduct. Targeted Ther.* 6 (1) (2021) 74.
- [5] J. Liu, et al., A METTL3-METTL14 complex mediates mammalian nuclear RNA N<sup>6</sup>-adenosine methylation, *Nat. Chem. Biol.* 10 (2) (2014) 93–95.
- [6] X.L. Ping, et al., Mammalian WTAP is a regulatory subunit of the RNA N<sup>6</sup>-methyladenosine methyltransferase, *Cell Res.* 24 (2) (2014) 177–189.
- [7] G. Jia, et al., N<sup>6</sup>-methyladenosine in nuclear RNA is a major substrate of the obesity-associated FTO, *Nat. Chem. Biol.* 7 (12) (2011) 885–887.
- [8] C. Tang, et al., ALKBH5-dependent m<sup>6</sup>A demethylation controls splicing and stability of long 3'-UTR mRNAs in male germ cells, *Proc. Natl. Acad. Sci. U.S.A.* 115 (2) (2018) E325–e333.
- [9] N. Liu, et al., N(6)-methyladenosine-dependent RNA structural switches regulate RNA-protein interactions, *Nature* 518 (7540) (2015) 560–564.
- [10] B. Wu, et al., Molecular basis for the specific and multivalent recognitions of RNA substrates by human hnRNP A2/B1, *Nat. Commun.* 9 (1) (2018) 420.
- [11] K.D. Meyer, et al., 5' UTR m(6)A promotes cap-independent translation, *Cell* 163 (4) (2015) 999–1010.
- [12] Z. Miao, et al., Evolution of the RNA N(6)-methyladenosine methylome mediated by genomic duplication, *Plant Physiol.* 182 (1) (2020) 345–360.
- [13] T.L. Bale, Epigenetic and transgenerational reprogramming of brain development, *Nat. Rev. Neurosci.* 16 (6) (2015) 332–344.
- [14] A.Z. Huang, A. Delaidelli, P.H. Sorensen, RNA modifications in brain tumorigenesis, *Acta Neuropathol Commun* 8 (1) (2020) 64.
- [15] A.M. Shafik, et al., N<sup>6</sup>-methyladenosine dynamics in neurodevelopment and aging, and its potential role in Alzheimer's disease, *Genome Biol.* 22 (1) (2021) 17.
- [16] M.J. Armstrong, et al., Diverse and dynamic DNA modifications in brain and diseases, *Hum. Mol. Genet.* 28 (R2) (2019) R241–r253.
- [17] H. Shi, et al., m(6)A facilitates hippocampus-dependent learning and memory through YTHDF1, *Nature* 563 (7730) (2018) 249–253.
- [18] T. Du, et al., RNA demethylase Alkbh5 is widely expressed in neurons and decreased during brain development, *Brain Res. Bull.* 163 (2020) 150–159.
- [19] Y.P. Yen, J.A. Chen, The m(6)A epitranscriptome on neural development and degeneration, *J. Biomed. Sci.* 28 (1) (2021) 40.
- [20] R. Zhang, et al., RNA N<sup>6</sup>-methyladenosine modifications and its roles in Alzheimer's disease, *Front. Cell. Neurosci.* 16 (2022) 820378.
- [21] F. Zhao, et al., METTL3-dependent RNA m(6)A dysregulation contributes to neurodegeneration in Alzheimer's disease through aberrant cell cycle events, *Mol. Neurodegener.* 16 (1) (2021) 70.
- [22] J. Widagdo, et al., Experience-dependent accumulation of N<sup>6</sup>-methyladenosine in the prefrontal cortex is associated with memory processes in mice, *J. Neurosci.* 36 (25) (2016) 6771–6777.
- [23] Z. Xu, et al., Efficient strategies for microglia replacement in the central nervous system, *Cell Rep.* 32 (6) (2020) 108041.
- [24] S. Jawhar, et al., Motor deficits, neuron loss, and reduced anxiety coinciding with axonal degeneration and intraneuronal A $\beta$  aggregation in the 5XFAD mouse model of Alzheimer's disease, *Neurobiol. Aging* 33 (1) (2012) 196.e29–196.e40.
- [25] R. Li, et al., Deep brain stimulation of fornix for memory improvement in Alzheimer's disease: a critical review, *Ageing Res. Rev.* 79 (2022).
- [26] R. Guerreiro, et al., TREM2 Variants in Alzheimer's Disease, 2013, p. 368.
- [27] X. Li, et al., Transcriptional and epigenetic decoding of the microglial aging process, *Nat Aging.* 3 (10) (2023).
- [28] S. Forner, et al., Systematic phenotyping and characterization of the 5xFAD mouse model of Alzheimer's disease, *Sci. Data* 8 (1) (2021) 270.
- [29] E. Griggs, et al., Recapitulation of pathophysiological features of AD in SARS-CoV-2-infected subjects, *Elife* 12 (2023).
- [30] X. Jiang, et al., The role of m<sup>6</sup>A modification in the biological functions and diseases, *Signal Transduct. Targeted Ther.* 6 (1) (2021) 74.
- [31] M. Zhuang, et al., YTHDF2 in dentate gyrus is the m(6)A reader mediating m(6)A modification in hippocampus-dependent learning and memory, *Mol. Psychiatr.* 28 (4) (2023).
- [32] B. Martinez De La Cruz, et al., m(6) A mRNA methylation in human brain is disrupted in Lewy body disorders, *Neuropathol. Appl. Neurobiol.* 49 (1) (2023) e12885.
- [33] A.M. Gocher, C.J. Workman, D.A.A. Vignali, Interferon- $\gamma$ : teammate or opponent in the tumour microenvironment? *Nat. Rev. Immunol.* 22 (3) (2022) 158–172.
- [34] R.S. Apte, D.S. Chen, N. Ferrara, VEGF in signaling and disease: beyond discovery and development, *Cell* 176 (6) (2019) 1248–1264.
- [35] A. Geremia, et al., Innate and adaptive immunity in inflammatory bowel disease, *Autoimmun. Rev.* 13 (1) (2014) 3–10.
- [36] E. Zenaro, et al., Neutrophils promote Alzheimer's disease-like pathology and cognitive decline via LFA-1 integrin, *Nat. Med.* 21 (8) (2015) 880–886.
- [37] J.K. Thurlow, et al., Spectral clustering of microarray data elucidates the roles of microenvironment remodeling and immune responses in survival of head and neck squamous cell carcinoma, *J. Clin. Oncol.* 28 (17) (2010) 2881–2888.
- [38] M. Schumacher, et al., Steroid hormones and neurosteroids in normal and pathological aging of the nervous system, *Prog. Neurobiol.* 71 (1) (2003) 3–29.
- [39] K.J. Grande-Allen, et al., Glycosaminoglycan synthesis and structure as targets for the prevention of calcific aortic valve disease, *Cardiovasc. Res.* 76 (1) (2007) 19–28.
- [40] G.T. Norris, J. Kipnis, Immune cells and CNS physiology: microglia and beyond, *J. Exp. Med.* 216 (1) (2019) 60–70.
- [41] A. Deczkowska, et al., Disease-associated microglia: a universal immune sensor of neurodegeneration, *Cell* 173 (5) (2018) 1073–1081.
- [42] V. Kalamani, et al., The role of the fat mass and obesity associated gene (FTO) in breast cancer risk, *BMC Med. Genet.* 12 (2011) 52.
- [43] H. Huang, et al., Altered expression of the m<sup>6</sup>A methyltransferase METTL3 in Alzheimer's disease, *eNeuro* 7 (5) (2020).
- [44] H. Lee, et al., Stage-specific requirement for Mettl3-dependent m<sup>6</sup>A mRNA methylation during haematopoietic stem cell differentiation, *Nat. Cell Biol.* 21 (6) (2019) 700–709.
- [45] F. Zhao, et al., METTL3-dependent RNA m<sup>6</sup>A dysregulation contributes to neurodegeneration in Alzheimer's disease through aberrant cell cycle events, *Mol. Neurodegener.* 16 (1) (2021) 70.
- [46] M. Han, et al., Abnormality of m<sup>6</sup>A mRNA methylation is involved in Alzheimer's disease, *Front. Neurosci.* 14 (2020) 98.
- [47] M.M. Varnum, T. Ikezu, The classification of microglial activation phenotypes on neurodegeneration and regeneration in Alzheimer's disease brain, *Arch. Immunol. Ther. Exp.* 60 (4) (2012) 251–266.
- [48] J. Du, et al., N(6)-Adenosine methylation of Socs1 mRNA is required to sustain the negative feedback control of macrophage activation, *Dev. Cell* 55 (6) (2020) 737–753.e7.
- [49] L. Wen, et al., The m<sup>6</sup>A methyltransferase METTL3 promotes LPS-induced microglia inflammation through TRAF6/NF- $\kappa$ B pathway, *Neuroreport* 33 (6) (2022) 243–251.
- [50] S. You, et al., Research progress on the role of RNA m<sup>6</sup>A modification in glial cells in the regulation of neurological diseases, *Biomolecules* 12 (8) (2022).